AIAA Scitech 2024 Forum, 8-12 January 2024, Orlando, USA, Paper number 2024-2861
DOI: 10.2514/6.2024-2861

Hypersonic boundary layer reduction with optimisation of the Hyshot II intake using numerical methods

Sam P. S. Burrows *, Zeeshan A. Rana † and Simon Prince ‡
Centre for Aeronautics, Cranfield University, Cranfield, Bedfordshire, MK43 0AL, UK

The Hyshot project demonstrated that the quality of flow in a scramjets combustion chamber is essential to achieve critical mass flow condition in a small profiled supersonic combustion chamber. This investigation utilises a steady RANS and real gas thermal model to explore boundary layer growth over various comparable compression ramp profiles in a hypersonic freestream condition. The results in this investigation suggested that given a constant net flow deflection angle and ramp length, the displacement thickness developing on a hypersonic compression ramp is inversely proportional to the magnitude of static pressure the ramp produces at the wall, where the highest pressures theoretically achievable are that of an isentropic compression process. A quasi isentropic compression distribution was achieved when the rate of deflection along a ramp's length is linear. The data collected also suggests that the difference in displacement thickness growth of the quasi isentropic ramp relative to the nominal flat plate increases as the flight Reynold's number increases, where the displacement thicknesses has the potential to reduce by over 50% relative to an equivalent flat plate. Low Reynold's numbers have found to yield the opposite effect, where isentropic turning of a hypersonic flow may increase the difference in these cases. Such reductions have been shown to theoretically allow for a critical mass flow rate in a two dimensional scramjet combustion chamber without requiring slot bleed systems, whilst achieving the required flow conditions for the auto-ignition of hydrogen. It is suggested that a scramjet design based upon these findings would still require some form of porous bleed system to compensate for the growth in the boundary layer as it expands about the compression ramp into the combustion chamber, which has potential to be incorporated onto an axisymetric design to optimise the effective mass flow rate per body diameter.

I. Nomenclature

A	=	Constant of wall heating described by Stollery
C	=	Constant of viscosity
M_∞	=	Freestream Mach number
P	=	Ratio of local static pressure to farfield conditions
Re	=	Reynold's number
T_w	=	Static wall temperature
T_0	=	Flow total temperature
δ^*	=	Boundary layer displacement thickness
η_{th}	=	Thermal efficiency of combustion
$\bar{\chi}$	=	Viscous interaction parameter

*Researcher, Centre for Aeronautics, Cranfield University, Cranfield, Bedfordshire, MK43 0AL, UK
†Senior Lecturer in Aerodynamics, Centre for Aeronautics, Cranfield University, Cranfield, Bedfordshire, MK43 0AL, UK
‡Professor in Aerodynamics, Centre for Aeronautics, Cranfield University, Cranfield, Bedfordshire, MK43 0AL, UK.

Published by AIAA. This is the Author Accepted Manuscript issued with: Creative Commons Attribution Non-Commercial License (CC:BY:NC 4.0).
The final published version (version of record) is available online at DOI:10.2514/6.2024-2861. Please refer to any applicable publisher terms of use.

II. Introduction

Supersonic intakes were first conceived by René Lorin in 1913, where a patent was issued in 1928 for the first modern ramjet engine [1]. The first powered flight using a ramjet engine was conducted in 1949 designed by René Leduc, proving the concept for use in supersonic propulsion.

Major progression into scramjet research occurred during the mid 20^{th} century, where the NASP program was developed in the United States with the aim of achieving flight to orbit. The project was scrapped in 1993 when the cost of completion was believed to be too great. NASA produced the X-43 program which aimed to incorporate scramjet technology onto a hypersonic cruising vehicle, tests are believed to have been unsuccessful.

The first successful scramjet flight test was then conducted by the University of Queensland in the Hyshot II in 2002, leading to increased interest from multi-national organisations and the research has subsequently gone behind closed doors for use in the defense sectors.

The Mass Flow Rate, MFR, in supersonic intake is typically referred to as the ratio of the streamlines cross sectional area entering the intake, with that of the maximum mass flow rate allowable given a shock-cowl engagement, visually shown below, as shown:

$$MFR = \frac{\dot{M}_i}{\dot{M}_\infty}$$

From this, it can be seen that choking the flow at the intake (reducing the effective mass flow rate) generates a large back pressure at the throat, which causes a normal shock before it. This subcritical operating condition reduced optimal total pressure recovery across the intake since freestream flow has not been decelerated in design conditions. A large, developed boundary layer at the external compression stage creates an effective body at the intake, reducing velocities close to the wall and therefore mass flow. This boundary layer can act to choke the flow at an intake and cause subcritical operation, known as an unstart condition for a supersonic intake. The conditions for successful scramjet operation are outlined as such.

A. The requirements for scramjet operation

1. Mass flow rate

A scramjet does not experience a supercritical condition, unlike a ramjet, since the intake does not require the formation of a normal shock, therefore the mass flow rate in any scramjet engine should be optimised as to reduce the likelihood of an unstart condition, and increasing flow rate to the combustion chamber and therefore optimising the thrust that the scramjet engine is capable of generating. From this, its suggested that the combustion chamber's effective mass flow rate should exceed 90% that of the equivalent freestream conditions.

2. Compression

High compression is essential for effective fuel mixing and combustion in all forms of jet power. Typical compression ratios in supersonic inlets exceed 60 times that of static freestream pressures. Fuel consumption is found to decrease with increasing compression ratios [2]. The thermal efficiency of combustion was also studied and was found to increase with compression ratio also. For the case of a scramjet inlet, high compression ratios should not be a limiting factor since a high freestream Mach number ensures that shock generation will create large compression ratios.

3. Temperature

Typically to optimise the thermal efficiency of combustion, the temperature of the upstream air should be minimised, as shown from the equation for thermal efficiency in combustion:

$$\eta_{th} = \frac{T_{01} - T_{02}}{T_{01} - T'_{04}}$$

However, a scramjet is uniquely restricted by the need to auto-ignite Hydrogen fuel injected into the combustion chamber. The static temperature for which Hydrogen is expected to self ignite in nominal conditions is 800K [3], therefore the intake is required to generate this condition downstream of mixed compression for successful scramjet operation.

4. Transition

Through investigation of published literature, its found that a turbulent boundary layer is required for the combustion chamber since this will ensure adequate air/fuel mixing. A turbulent boundary layer however is known to have a larger displacement thickness than a laminar however so this must be addressed in any design to prevent unstart.

B. Modern Boundary layer bleed devices

It is essential to reduce the thickness of the boundary layer in all supersonic intakes as to ensure critical operation, and stable shock formations on the design criteria. Through this, much research has been conducted in the form of different boundary layer suction techniques as well as their effectiveness in context. A boundary layer suction slot was first applied to a supersonic intake in 1944 in Oswatitsch's work, who was one of the main collaborators to such technologies. The four main configuration types include a choice of a porous or slot bleed, that's integrated as a ramp or flush system. The choice and implications for each design is somewhat clear, wherein a slot bleed allows for a large mass flow rate bleed whereas a porous slot is more restrictive; therefore, in regions of known separation and boundary layer growth a slot is typically employed as it may be effectively optimised to offset local flow separation whilst mitigating negative effects of its implication. A porous bleed slot is then employed in regions of unstable flow fields, where a small and generic mass flow bleed is required to either offset transition, or reduce boundary layer thicknesses upstream of some key point.

C. The Hyshot II

The Hyshot project was developed by Australia's Centre for Hypersonics at the University of Queensland with the aim of developing the capabilities for supersonic combustion. It's widely believed that this project produced the first successful scramjet combustion flight test, which has led to two decades of follow up projects and development following numerous national collaborations upon its success. The first successful scramjet test flight was conducted in August 2002, with a data duration of 10 seconds and a maximum speed of Mach 7.95, where it was found supersonic combustion had been achieved [4]. This had been the first step in validating ground test data, which consolidates the methods for further hypersonic engine development.

Official collaboration between US and Australian defence research departments; DARPA and DSTO respectively occurred with the HyCAUSE program to further development. This was further evolved into the HIFiRE project, where collaboration between DSTO and the US Air Force research laboratory, as well as commercial involvement from Boeing to develop this research into a defence weapons system [5]. Naturally, detailed publications have not been released in terms of technical analysis since Hyshot II, leading to the motivation for this project.

Since the last published successful scramjet design in the Hyshot program is the Hyshot II, this project will focus on design optimisation based upon this model - whilst attempting to retain features that made that design successful, learning from the failings of the HyCAUSE design. Below describes the intake and combustion chambers side profile dimensions for the Hyshot II.

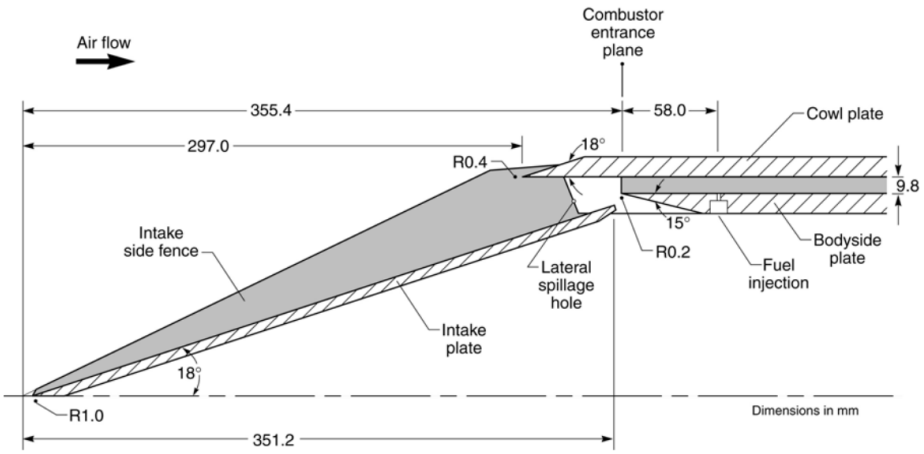

Fig. 1 Hyshot II side profile geometry definition for the flight test [6].

This design was created with the goal of simply achieving supersonic combustion. It features a simplified geometry consisting of a single compression ramp and an axially parallel cowl [7]. Since boundary layer growth is the major factor in choking scramjet engines, this was overcome through use of a large ram slot immediately upstream of the combustion chamber. Moreover, bleed slots were created on the combustion chambers entrance side walls to reduce shock-boundary layer and shock-shock interaction interference's. This design was created to generate a near 2 dimensional flow field in the combustion chamber to allow for easier analysis of the flow field and combustion. Such designs however are restrictive in terms of flow manipulation and mass flow rate has not been optimised in this design. The ram bleed will severely reduce the combustion chambers mass flow rate as well as generating less than optimal flow conditions on the outer side walls of the intake, increasing the designs net drag and destabilising the craft in this case, perhaps causing the oscillatory action found in the flight data which must be addressed.

The data found in the Hyshot II project will be used to calibrate the numerical solver to be used in this project, wherein a 2D solver will be used as well as a mesh convergence study to validate the meshing and solver to be used in subsequent design optimisations.

Time (s)	M_∞	q_∞ **(kPa)**	h_p **(Km)**	α **(deg)**
538.103	7.828	24.88	34.48	-5.012
538.179	7.831	25.33	34.31	5.540
538.734	7.938	31.55	33.05	-5.081
538.805	7.938	32.20	32.89	4.617

Table 1 Freestream flight characteristics for the Hyshot II flight test [6].

Time (s)	P_c **(kPa)**	T_c **(K)**	M_c	$\dot{m}$ **(kg/s)**
538.103	39.586	1305.90	2.604	0.1416
538.179	25.215	921.08	3.457	0.1440
538.734	50.530	1306.40	2.600	0.1713
538.805	34.130	943.50	3.390	0.1775

Table 2 Unfuelled combustor entrance characteristics for the Hyshot II flight test [6].

D. Analytical methods for boundary layer prediction

Two analytical methods for predicting boundary layer growth are outlined in this project as a means of validating the numerical solutions. Firstly, John Stollery and Lorraine Bates explored the effects of strong interaction, and described a method for determining these factors analytically in their paper of turbulent hypersonic viscous interactions in 1974 [8]. Its understood that the effective body shape is a function of the displacement thickness, of which is a function of the static pressure field; which in turn is a function of the effective body. Stollery and Bates described the following relation to combine these factors:

$$M_\infty \frac{\delta^*}{x} = A\bar{\chi}_{lam}\left(\frac{1}{x}\int_0^x P\, d\xi\right)^{0.5}/P$$

Wherein:

$$A = 0.664\left(\frac{\gamma - 1}{2}\right)\left(1 + 2.6\frac{T_w}{T_0}\right)$$

$$\bar{\chi} = M_\infty^3\sqrt{\frac{C_\infty}{Re_x}}$$

$$P = \frac{P_e}{P_\infty}$$

Secondly, the idea of local flat plate similarity describes that a boundary layer developing on a ramp is equivalent to that of a flat plate at incidence, yielding the following:

$$\frac{\delta^*}{x} \approx \sqrt{\frac{C_1}{Re_x}\frac{M_1^2}{P}}$$

E. Objectives and structure

The objective of this project is to ascertain whether the intake's need for a large boundary layer ram bleed duct may be neglected, or exchanged for a simplified system, through gradually turning freestream flow; reducing overall shock strength and therefore the boundary layer's thickness. This techniques feasibility will be considered against practical design considerations, as well as its reliability for use on a ballistic flying body. The thought being that the current ram bleed system does not allow for an axisymmetric geometry, which is essential for optimising the mass flow rate in a limited cross-sectional area, such as the case for an air breathing missile body.

The qualified objectives therefore are to, within the bounds of feasible design, determine whether turning a Mach 8.0 flow gradually reduces the overall boundary layer thickness on a two dimensional flow case. Secondly, for the case that boundary layer reduction is successful, examine whether this is impacted by flight Reynold's number and wall temperature. Finally, determine whether a simplified boundary layer bleed technique may be employed to an axisymmetric geometry, and whether this achieves sufficient quality flow for use in the supersonic combustion of hydrogen.

III. Computational Framework

A. Meshing Strategy

1. Defining the blocks

Using the software Ansys ICEM, a blocking structure is firstly established to base the structured mesh from. Several forms of the blocking structure were explored to best capture the geometry where the finalised structure is displayed in Fig. 3.

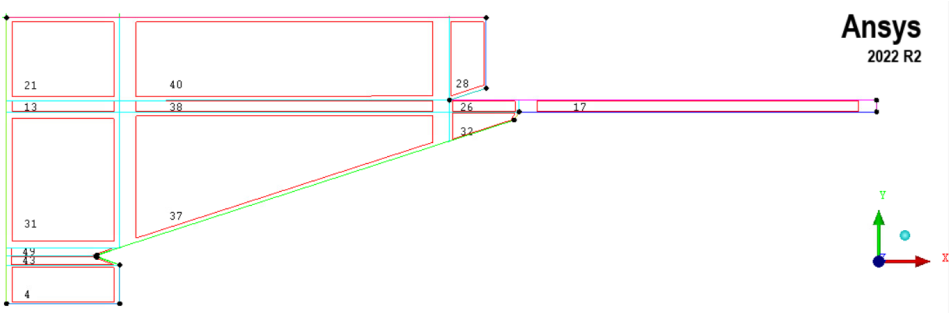

Fig. 2 Mesh blocking structure for the Hyshot II geometry to be used in the numerical validation study.

The benefits of this meshing technique are apparent from the blocking structure, since it allows for a highly regular and Cartesian dominant mesh to exist in the combustion chamber, alongside aligned mesh elements on the compression ramp [9]. This method also allows for a greatly controllable mesh density in each area of the boundary, where a coarser structure may be enabled in regions of lesser importance, such as the underside of the nose and above the cowl.

Curvature about the nose posed some issues when generating this mesh scheme, and this blocking structure appears to compromise the best at capturing the curvature, and minimising skew on downstream elements. However, the stitching of elements between edges must be treated with caution, and this method leaves a lot of room for elements not matching about nodes, which can cause loss in grid quality if not handled correctly.

2. Node definition

Upon generating the structured mesh, node definition is an essential part of capturing the boundary layer, wherein the Y+ value at the wall defines the resolution of the viscous sublayer with respect to the flow conditions, and each turbulence model requires different levels of resolution for full convergence. All meshes used in this study are constructed to a resolution of $Y^+ = 1$, since this is the highest level of resolution in common turbulence models and is that required for the $K - \omega$ *SST* solver. The first cell height in the mesh that can achieve this value is quickly estimated since the Y^+ in a simulation is defined as [10]:

$$Y^+ = \frac{y\mu_\tau}{\nu}$$

Where,

- y is the absolute distance above the wall, the variable required to construct the mesh.
- μ_τ is the friction velocity defined as $\sqrt{\frac{\tau_w}{\rho}}$
- ν is the dynamic viscosity of the flow

The shear stress at the wall, τ_w, may be estimated using:

$$\tau_w = \frac{C_f \rho U_\infty^2}{2}$$

And the coefficient of friction:

$$C_f = \frac{0.026}{Re_x^{\frac{1}{7}}}$$

To calculate a desired Y^+ value of 1 as a minimum requirement for the SST turbulence model to achieve resolution of the viscous sublayer, it was found that the first node height is required to be $y_1 = 0.00015$ with an estimated appropriate sizing ratio of 1.1, where it is defined as 0.0001 in the mesh to account for numerative and modelling error, as well as it to be used in further study with different flow cases.

With this first node height and blocking structure, an ultra coarse mesh is defined to highlight issues with the mesh, displayed in Fig. 4.

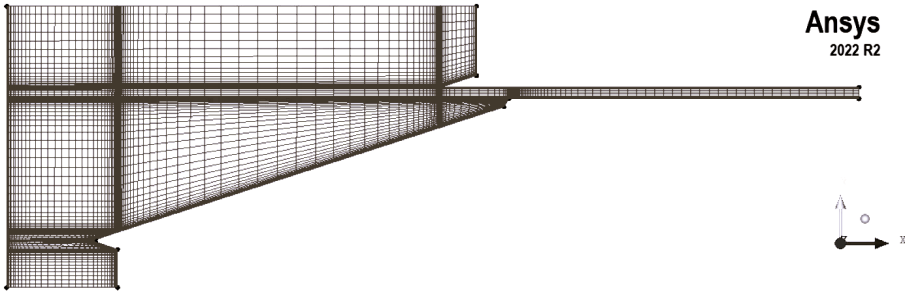

Fig. 3 Ultra coarse Hyshot II mesh.

Upon examination, it was found that the node spacing across edges must have matched to achieve an consistent element spacing and global mesh. This caused excellent geometry definition at key locations of the mesh such as the cowl and blunted nose, but the stitching meant that there were quite some wastage of element density, particularly towards the upper left side of the mesh where high density was not required. Nevertheless this method requires a very low number of elements for solution convergence so it was determined that the method is still valid for use in this investigation.

3. Mesh analysis

Increasing the number of nodes from this points allow for a final mesh to be generated for analysis. Three meshes were generated for a convergence study; coarse, medium and fine with the number of elements 150240, 300600 and 600102 respectively. Appendix 3 describes the mesh metrics for the medium mesh which similarly describe the three mesh densities.

Its shown that the minimum mesh quality is 0.95, which validates this mesh technique for generating an even and consistent grid for use in a numerical simulation. Despite this, the mesh exhibits a number of skewed elements about the nose and node stitching points as was expected, this effect is on a relatively small number of elements but the skew is limited to a minimum magnitude of 0.15, limiting its adverse effects. Fig 5 show the area of the medium mesh where the skewness is most affected.

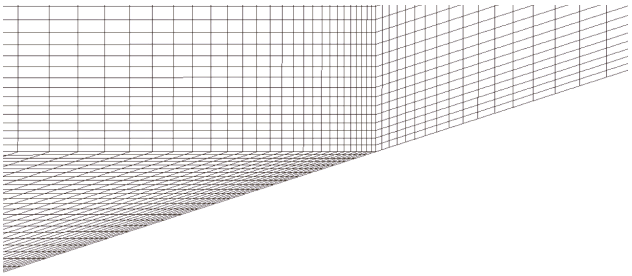

Fig. 4 The Hyshot II medium mesh edge stitching downstream of the nose.

The skewness of these elements causes a loss in orthogonal quality for the global mesh which can be seen in the metric plots, again the effect is limited when considering the global mesh and is deemed acceptable for this type of study since its found to be unavoidable. The high density of elements at the nose should allow for a well defined and converged flow field at this point which should serve to counter these lower quality elements.

Furthermore, the aspect ratio of the elements experiences a predictable linear increase as a result of the resolution at the boundary layer. To try to combat this would be to increase the longitudinal number of nodes on each edge which is not necessary for solution convergence and will produce too many elements for its value, these aspect ratios are expected in any numerical solver that resolves viscous sublayers and should not affect the solver performance.

Whilst the first cell layer height may ensure that the turbulence model used in a simulation can be resolved, the number of cells in a boundary layer must still be sufficient to converge the solution through the different layers of a turbulent boundary layer in particular. It was determined visually that the mesh used for the fine density simulations comprised of 60 to 200 number of cells normal to the wall in the boundary layer along the length of the ramp. It could be construed that this is suitable resolution to ensure that the expansion ratio between elements is sufficient to capture the boundary layer effectively.

Overall, despite the loss in mesh density efficiency and element skewness, the final meshes produced appear to be fit for purpose, with a consistent makeup and conforming to the geometry. Its believed that this mesh satisfied the initial requirements outlined at the beginning of this section, with most application at capturing the true flow field calculated from the solver, with good metrics and the ability to extrude the mesh into a 3D boundary if required.

B. Boundary conditions

The software used in this investigation is the Simcenter Star CCM+ solver program. This choice was made as to benefit from the real gas solvers that are installed to capture the high temperature gas flows that are expected in the flow regime as it had been determined that the maximum temperatures the flow field could experience would exceed that an ideal gas assumption could capture. The following described the domain's boundary conditions used in all simulations.

Wall: The wall conditions were set up with the typical no-slip condition, aerodynamically smooth as well as the adiabatic thermal property, which models zero thermal transfer to and from it, acting as a perfect insulator.

Farfield out, bleed slot, combustor out: The conditions at the pressure outlet boundaries were set up to be a function of the local flow parameters, namely Temperature and pressure. Backflow specifications were extrapolated by environmental parameters where the turbulence intensity for all simulations is a constant of 0.01 with a turbulent viscosity ratio of 10, which is found to work best with the gamma transition model.

Farfield: The farfield was defined by freestream parameters, chosen to match that of a stable data set from the experimental flight tests for comparison: Mach number=7.95, Temperature=231.8 K, Pressure=715.29 Pa, Mach components=[cos(5),-sin(5)]. The freestream conditions are given an angle of attack of -5 degrees as was found in the flight tests that experienced unsteady oscillations through testing.

Solver Configuration

The solver was found to be unstable in many circumstances, where solution divergence and unsteady behaviour was typical for many computational configurations. This is believed to be the case since a highly compressible flow field is intrinsically unstable, and performing a RANS simulation on such a flow field may cause large discretisation errors close to the wall, which are exacerbated by large pressure gradients and therefore internal stresses on the fluid. The averaging of two adjacent cells was impossible to stabilise for an explicit solver in this case, independent of the mesh density; the following describes the technique for achieving reliable and repeatable solutions in this hypersonic flow field on a RANS solver.

It was found to be useful to run the following with a first order truncation on an inviscid solver, allow for convergence and then apply the turbulence model with a second order discretisation since this allowed the global flowfield to develop without inviscid displacement and was found to converge the viscous solution much more predictably with more stability.

Gas properties: The standard air model was employed with Sutherland's law of viscosity and thermal conductivity, constant molecular weight as well as the equilibrium air model to be used to calculate its local ratio of specific heats. This model is validated for use in this investigation since at standard atmospheric pressure, the relaxation time for vibrational and dissociative energies are on the order of $\approx 10^{-4}$ and $\approx 10^{-6}$ seconds respectively. When the flow on the ramp itself is roughly 2222 m/s, the maximum distance of inert degrees of freedom for the gas to dissipate to the equilibrium model distributions of energy is $10^{-4} * 2222 = 0.22m$, since the ramp is 350mm in length the combustion chamber flow will experience a gas that conforms to the equilibrium air model, and as such is suitable for use in this investigation.

Coupled flow: The coupled flow solver was chosen which computes the conservation of continuity and momentum simultaneously. As stated this is used with an implicit, AUSM+ FVS inviscid flux, where the time step is CFL is controlled automatically to achieve the target. This adds stability to the AMG solvers convergence and is useful to this particular flow field [11].

Gamma transition: The gamma transition model in CCM+ solve additional transport equations in the boundary layer coupled with the SST turbulence model, and are said to provide a true prediction capability to transition with the solver. This was employed since transition prediction is difficult to achieve with lower fidelity methods for a hypersonic flow regime, and this will be helpful to asses how different ramps affect transition in future study.

Turbulence modelling: As assessed, the turbulence model to be used is the $K - \omega$ SST since it provides the most accurate results in the two dimensional simulation when compared to experimental data available. Convection is second order truncated alongside compressibility corrections.

RANS: As stated, hypersonic flows are inherently unstable due to the large internal stresses and forces such a flowfield may exert. It might be inferred that a solver that can capture the unsteady behaviour would be more useful than that of a RANS solver. Despite this, the study is interested in global boundary layer development, and a time averaged solution may provide more insight into the general trends of the effects to be investigated since the unstable nature of the flow is not at interest for this project, the stable flow in the cruising flight of a scramjet engine is of interest and therefore a steady RANS solver will provide the most useful data for analysis in this case.

IV. Results

A. Solver validation

1. Grid Convergence Index

Before analysis may be conducted on the solution a numerical simulation produces, that solution itself must be verified as converged in terms of the mesh used in the computation. There is no generally accepted method for conducting this validation, however it is acknowledged that examining the discretisation error between successive grid densities as described by Roache in the ASME Journal of Fluids Engineering [12] is a good form of mesh density validation.

This method describes that as the spatial grid is refined, the discretisation error asymptotes to zero, neglecting truncation error in the simulation. The flow parameter to be used in this study is density since this was determined to best express the stability of the solver as it is a result of both pressure and temperature in the flow.

Grid spacing's were chosen with base two relative magnitudes by tradition. The location chosen for analysis was the normal centre of the combustion chamber, in the middle of the first shock triangle as a stable part of the flow field is required for analysis; this corresponds to the global Cartesian coordinates of [0.38,0.125] in metres. Conducting this yields the following results:

Firstly, to calculate the order of convergence, p:

No. Elements	Grid normalised	Relative grid spacing	$\rho[kgm^{-3}]$
600,102	1	1	0.14089
300,600	2	2	0.14071
150,240	3	4	0.13597

Table 3 Density values for each mesh refinement to determine the grid refinement index.

$$p = ln(\frac{\rho_3 - \rho_2}{\rho_2 - \rho_1})/ln(r) = 4.77966$$

Where, r, is the constant of grid refinement; in this case $r = 2$. The theoretical asymptotic value of ρ may be determined with:

$$\rho_{h=0} \approx \rho_1 + \frac{\rho_1 - \rho_2}{r^2 - 1} = 0.14089739$$

The grid convergence index between each subsequent mesh may be calculated with:

$$GCI_{n,n+1} = \frac{F_s|\rho_n - \rho_{n+1}/\rho_n|}{r^p - 1} * 100\%$$

With the factor of safety, F_s, typically chosen as 1.25, the percentage of grid convergence between each mesh is calculated and the result displayed below:

$$GCI_{12} = 0.0008154\%$$

$$GCI_{23} = 0.0223976\%$$

Where finally the asymptotic range of convergence may be determined:

$$\frac{0.0223976}{2^{4.77966} * 0.0008154} = 1.000023615$$

When the above value is approximately one, it indicates that the value falls within the asymptotic range of convergence, where the density solution is 0.14089739 with an error band of 0.0224‰. Therefore, the medium mesh spacing will be used in this and further investigations as to balance solution time and convergence.

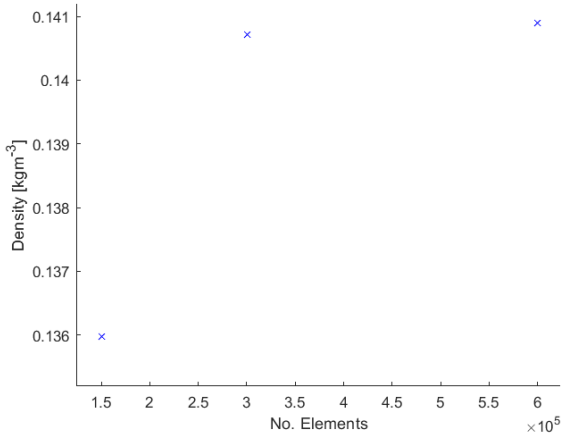

Fig. 5 Density plotted against number of elements in the GCI study.

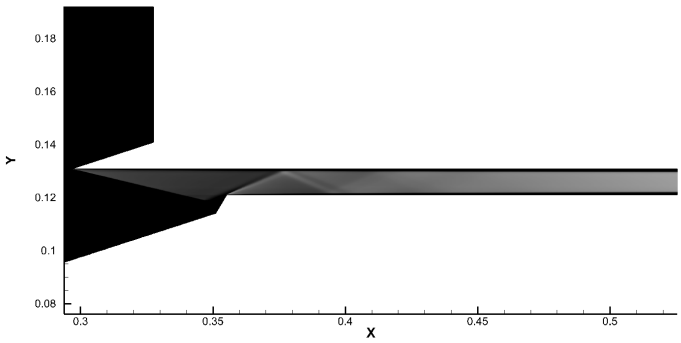

Fig. 6 Shadowgraph depicting the shock train in the combustion chamber for the fine mesh of the Hyshot II numerical solution.

2. Numerical solution validation with flight test data

The medium mesh was used to examine three RANS turbulence models to determine which one most closely matches to that of the experimental flight test data, where the flow was examined at [0.38,0.125] since this is the fuel injection port of the flight test where the data was collected as the combustor entrance.

	Flight test data	$K-\omega$ **SST**	**% diff.**	$K-\omega$ **STD**	**% diff.**	**Spalart Allmaras**	**% diff.**
AOA [deg]	-5.081	-5	-1.607	-5	-1.607	-5	-1.607
M_∞	7.938	7.95	0.15106	7.95	0.15106	7.95	0.15106
P_{comb} **[Pa]**	50530	53674.4	6.03514	54738.1	7.99497	53718.3	6.11679
T_{comb} **[K]**	1306.4	1338.5	2.42597	1345.53	2.95106	1354.3	3.60257
M_{comb}	2.6	2.63	1.29761	2.621	0.80416	2.606	0.22798
$\rho_{comb}[kgm^{-3}]$	0.13477	0.14072	4.31876	0.14278	5.7709	0.13921	3.24124

Table 4 Different turbulence models data collected at [0.38,0.125] with the percentage difference of each data point to that of the experimental set.

From these results, its apparent that in all cases, the static pressure is least accurately predicted from the simulations. Its hypothesised that pressures are over predicted due to the fact that the flow is not further choked as a result of the sidewalls, therefore velocities are slower than what would be in a three dimensional flow and thus static pressures are higher.

Furthermore, the SST model performs the best in predicting temperature and pressure, which are the most important parameters for assessing boundary layer development and thus will be chosen for use in further analysis.

As can be determined from the contour plots in Appendix D, the converged shock angle on the compression ramp is determined to be 25 degrees, an effective ratio of specific heats is claimed to be 1.25 as gathered from previous studies; and using this to calculate the theoretical shock angle of a sharp ramp of the same angle yields a shock angle of 28 degrees. A difference in modelling can be responsible for the discrepancy as the Hyshot models a blunted nose which is known to have the effect of reducing β.

Overall, the $K-\omega$ SST turbulence model alongside thee equilibrium air thermal gas solver appears to capture the complex hypersonic flowfield, with errors in key flow parameters ranging from 1.3-6.0%. Given these errors are following a series of complex shock interactions, a stagnation point at the nose and several chains of shocks, it can be determined that the solver is more than suitable for use in analysing boundary layer development across a series of simple ramps in the following investigation, with an expected upper bound error of ±6%.

3. The flowfield

The flowfield is visually assessed to produced the expected flow regime for the given domain. A curved bow shock is defined on the blunted nose with a clear discontinuity in pressure and density as expected. The temperature profile however describes a kinked profile at the nose. It is expected that this is a result of thermal radiation from the high stagnation temperatures at the nose predicted by the equilibrium air model employed in these simulations. Naturally these are not valid in the stagnation region, where the flow here would experience a non-equilibrium thermal regime -

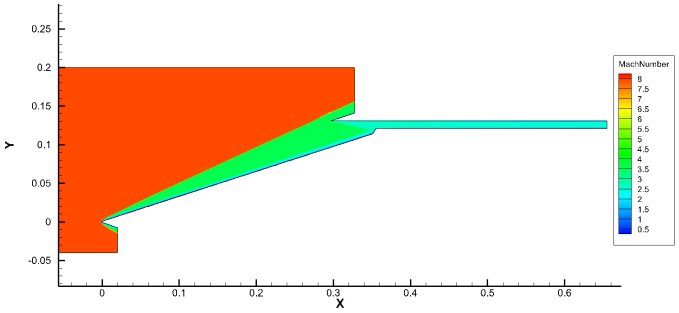

Fig. 7 Global Mach number contour for the Hyshot II fine mesh, Re=2E+05.

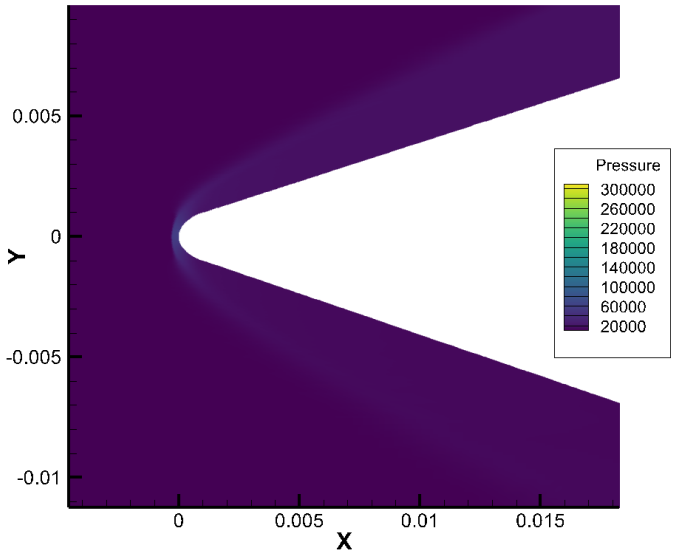

Fig. 8 Nose pressure contour for the Hyshot II fine mesh, 2E+05.

however the control for this validation is in the combustion chamber which does expect such a gas flow, as such the initial concern in the contours is mitigated.

Since the numerical configuration has been validated to accurately reflect the complex flow field and subsequent viscous developments in the case of the Hyshot II flight experiment; the same solver may be used to investigate how the boundary layer may develop given different ramp profiles and therefore pressure distributions, with expectation of reflecting closely to that of what would be observed in a real gas flow. It has been observed analytically that an isentropic pressure distribution has the potential to reduce both the boundary layer, and displacement thickness in relation to the constant pressure distribution a flat ramp theoretically provides. This investigation will aim to conclude to what extent this phenomena occurs alongside its applicability onto a scramjet compression spike with further analyses on the flowfield these techniques develop.

B. Ramp profile investigation

1. Investigation Definition

Aim: To determine whether the rate of change of a compression ramps local deflection angle reduces the displacement of a viscous hypersonic fluid, obtain an optimal case and explore the limitations of the phenomenon.

Independent Variables:

- Ramp length, $L = 350mm$

- Net flow deflection, $\theta_{net} = 18^o$
- Ramp discretisation, $dx = \frac{L}{18}$
- Mesh maximum node spacing = 1.00mm
- Reynold's number and solver configuration as described in 6.3.

Dependent variable:
- The rate of change of the local deflection angle on the compression ramp, $d\theta$.

Methodology
Firstly, define and construct four ramps to be used in the investigation, wherein a two dimensional domain used for the computations is meshed, using the same meshing technique as in Chapter 6 and run the solver as previously described until residual convergence. Subsequently, produce case files for each simulation and import them into Tecplot 360 EX 2022 R2, ensuring that the Mach, pressure and temperature contours are collected for each case. In all cases, obtain the boundary layer velocity profiles at x(mm)=[5, 10, 25, 50, 75, 100, 150, 200, 250, 300, 350]. This is achieved by generating polylines locally perpendicular to the wall at each location, and exporting 300 data nodes where the velocity magnitude and y values are exported and subsequently plotted. The y data should be normalised to the local ramp angle using $cos(\theta)$ to convert from global to local y units. From these velocity profiles, calculate the boundary layer, displacement and momentum thicknesses for each profile, as well as the shape factor at each location. From that, collect the temperature and pressure distributions on the wall in each case, as well as the wall Y+. Obtain pressure and temperature profiles normal to the wall at the end of each ramp to represent the flowfield that would enter the combustion chamber. Finally, plot all data and conclude trends shown. Relate how the formation of the boundary layer is correlated to the temperature and pressure at the wall and outline the suitability of the flowfield for use in a scramjet combustion chamber. Discuss whether this method is suitable for eliminating the need for a slot bleed in such a system and its application to the Hyshot program.

2. Ramp construction
A perfectly isentropic ramp would require an infinite length to achieve practically, since $d\theta \rightarrow 0$ in such a case. As such, for the purposes of this investigation the large number of variables that come with the definition of the ramp must be reduced to one for analysis. In this case, the ramp is constructed using a second order function to define the local ramp angle along its length, therein changing only the rate of change of the ramp angle along its length, which is found to be useful in reducing the complexity of its definition. The four ramps are defined in this manner with the following:

$$\begin{aligned} i. &\quad \theta = const. \\ ii. &\quad \theta = f(x) \\ iii. &\quad \theta = f(x^2) \\ iv. &\quad \theta = f(\sqrt{x}) \end{aligned}$$

Constraining the functions to all achieve a turning angle of $\theta = 18^o$ after 350mm, where the ramp is discretised into segments of $\frac{L}{18}$ appear as such:
Its hypothesised that $\theta = f(x^2)$ will yield the smallest boundary layer displacement since this ramp most closely resembles that of an isentropic ramp, and as such should yield the highest static pressures.

3. Data Processing
Following the methodology outlined above, boundary layer velocity profiles are obtained throughout the ramp. Firstly, the y data collected must be normalised with $y_{norm} = (y - y_{min}) * cos(\theta) * 1000$ so that the velocity magnitude may be plotted against the true y value perpendicular to the wall.
From these velocity profiles, the incompressible boundary layer thickness may be obtained through the definition [13]:

$$u_{y=\delta} = 0.99U$$

Where U is the velocity of the inviscid flowfield. The value of δ may be extrapolated from the corresponding data set of 0.99U. The displacement thickness is obtained through performing the following integration of the velocity profile [13]:

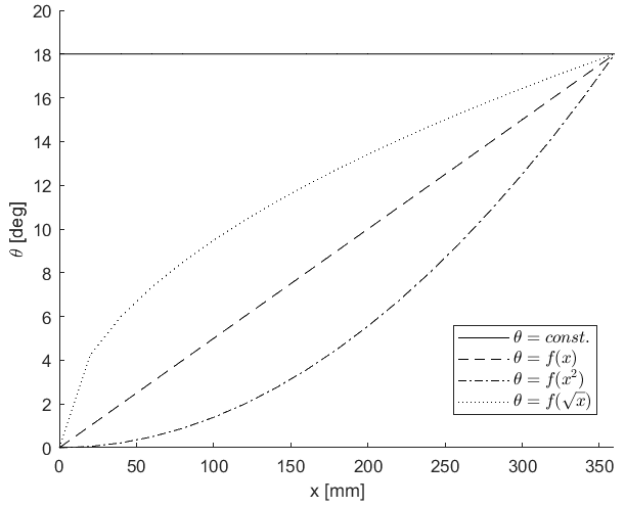

Fig. 9 Theta plotted against x defining each ramp profile to be used in the investigation.

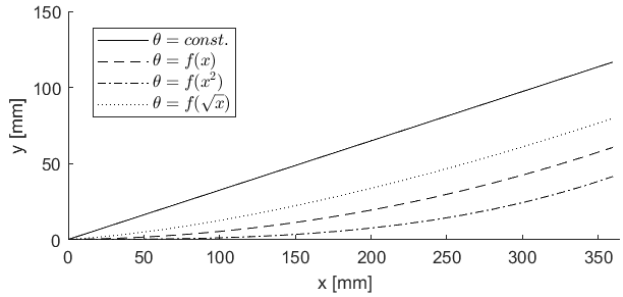

Fig. 10 Scaled y plotted against x defining each ramp profile to be used in the investigation.

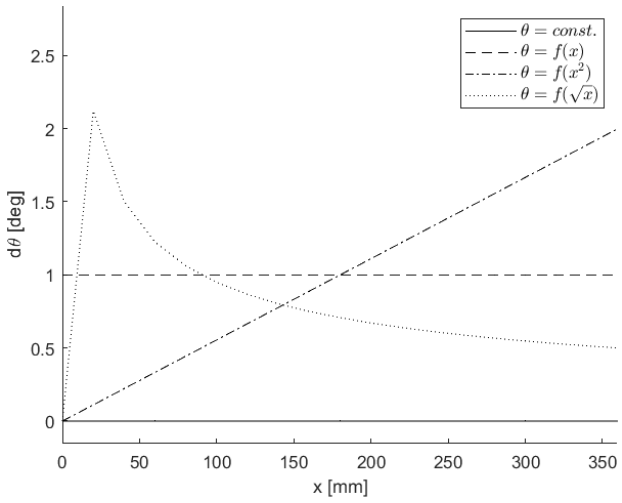

Fig. 11 $d\theta$ plotted against x for each ramp described in the investigation.

$$\delta^* = \int_0^{\delta} (1 - \frac{u}{U})\, dy$$

The momentum thickness of the boundary layer describes the similar displacement of the inviscid flowfield as δ^*, with

relation to the flows momentum rather than mass flow rate; and is described with [13]:

$$\theta_\delta = \int_0^\delta \frac{u}{U}(1 - \frac{u}{U})\, dy$$

From these, the shape factor, H, of the boundary layer may be obtained for each data set with the definition:

$$H = \frac{\delta^*}{\theta_\delta}$$

The shape factor is typically used to describe how the boundary layer reacts to the onset of an adverse pressure gradient as is found in the isentropic ramps in this investigation.
The integration's performed in this investigation were performed using the trapezium method of integration between data points. This was chosen rather than approximating the function that represents the velocity profile since each profile was compiled with 200 data points, as such the resolution was deemed suitable for such analysis. The trapezium method of integration imposes a second order truncation error into the calculation, since it calculates to the equivalent resolution of a first order calculation in the Taylor expansion, given below [14]:

$$f(x) = f(a) + \frac{f'(a)}{1!}(x - a) + \frac{f''(a)}{2!}(x - a)^2 ...$$

Where

$$f(x) = \int_0^x f'(y)\, dy$$

The trapezium method involves averaging the y value between two data points, and multiplying this by the change in x, as such where n is the number of data points:

$$\int_{y_{n-1}}^{y_n} f(u)\, dy \approx \sum_{n=1}^{n} \frac{y_n - y_{n-1}}{2} * (x_n - x_{n-1})$$

Determining boundary layer thickness in the strong interaction region
At the leading edge of a compression ramp, the viscous interaction between the thin shock and boundary layer meant that determining the thickness through means of analysing the velocity magnitude alone is difficult to achieve accurately as there is no clear asymptotic behaviour. Therefore another parameter should be used to determine the boundary layer thickness in this region. It was found that analysing the vorticity normal to the wall will distinctly show the different regions of flow, including the boundary layer. Parallel flow will still exhibit vorticity close to the wall as a result of shearing action between adjacent layers, plotting vorticity against a normalised y in the strong interaction region for the flat plate case is shown below.

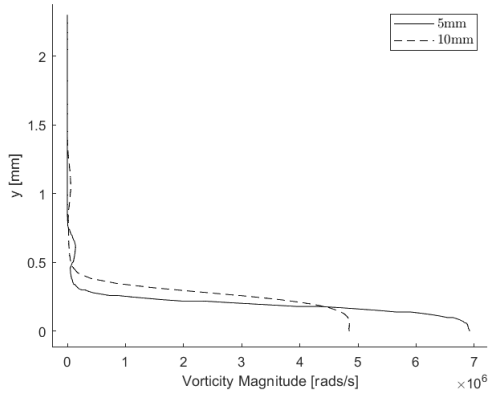

Fig. 12 Vorticity plotted normal to the wall in the strong viscous interaction region for the flat plate, Re=2E+05.

Vorticity asymptotes to a constant value close to the wall, where it reduces throughout the boundary layer in a linear fashion. In both the 5 and 10 mm profiles, a small bump may be observed in vorticity at the location of the shock wave. The boundary layer thickness is defined as the first point for which vorticity asymptotes to zero, defined at the farfield region.

4. Observations

Conditions at the wall

Below describes the wall temperature development for each ramp described in this investigation. This data should be analysed with respect to the fact that the wall is modelled with an adiabatic condition, wherein no thermal transfer occurs between the viscous fluid and itself. Therefore, the temperature at the wall is a result of the insulated heating caused by viscous interaction between the fluid and the wall, and as such represents the upper bound for what such a flow case could yield across the compression ramps, and does not reflect the true wall temperatures such a wall would experience. This data is useful however to compare the thermal heating each boundary layer generates relative to one another, where its seen that the flat ramp case generates by far the largest wall temperatures, whereas the isentropic ramps initially experience smaller wall temperatures, but accelerate rapidly as the flow is turned. From these plots, it is clear that isentropic turning may be an effective solution in reducing viscous heating in a hypersonic boundary layer, where the effect of wall temperature must be further investigated to understand the true effect of isentropic turning on wall temperature.

Fig. 17 describes the static pressure distribution along each ramp investigated. As expected, the flat ramp generates a near constant pressure field with a slight negative slope as the flow begins to recover from the initial oblique turning. Small numerical instability is observed in the first quarter of the flat ramp and is not indicative of the physical nature of the flow.

Its understood that the static pressure is constant throughout the boundary layer, therefore analysing the wall pressures indicated the local pressure in the flowfield each ramp generates. Its observed that each isentropic ramp generates much lower pressures, however higher than that which an inviscid solution would predict due to its displacement. The gradual turning however rapidly increases local pressures experienced by the developing boundary layer, where the f(x) ramp appears to generate the largest static pressures after an equal 18 degrees of flow deflection, closely followed by the parabolic ramp profile.

It's shown in this data that all isentropic ramp profiles generate a larger static pressure at the wall than the flat ramp case, where the sqrt ramp exhibits a marginally larger static pressure since the rate of flow deflection is significantly more abrupt than the other ramp cases, representing the profile closer to that of a flat ramp case.

It's also known that while the flat ramp will generate a uniform pressure field downstream of the oblique shock wave, the isentropic flow fields experience a varied pressure profile perpendicular to the wall, where the wall pressures are typically the highest experienced in the flow. The flow profiles in the isentropic ramps are highly influenced by the combination of mach or shock waves, which shape the region of disturbed flow and impact their attribute magnitudes.

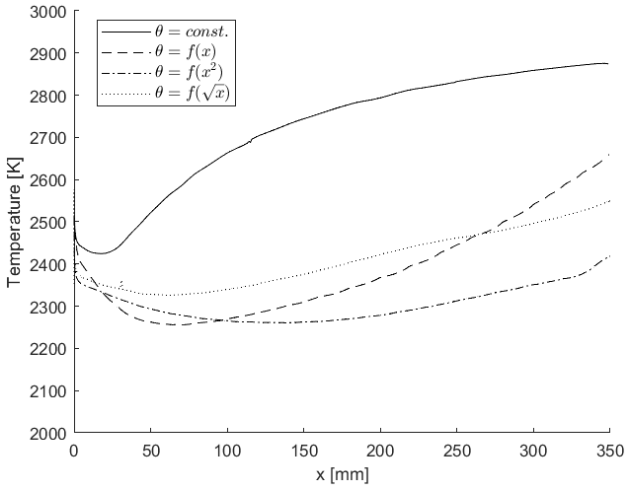

Fig. 13 Wall temperature plotted along the length of each ramp, 2E+05.

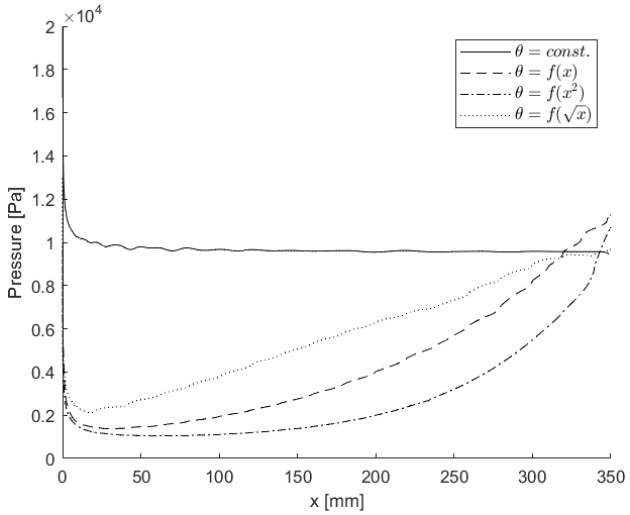

Fig. 14 Wall pressure plotted along the length of each ramp, 2E+05.

Transition

The γ-Re transition model employed in these investigations adds a transport variable into the turbulent model known as intermittency. It reacts in accordance to the production of turbulent kinetic energy in the simulation, and determines transition based on this. It was created to fit a large range of flow cases, and may provide an indicative solution as to when a flow regime will transition into turbulence. Fig. 18 and 19 describe the boundary layer velocity profiles for the flat ramp and linear rate of deflection ramp profiles.

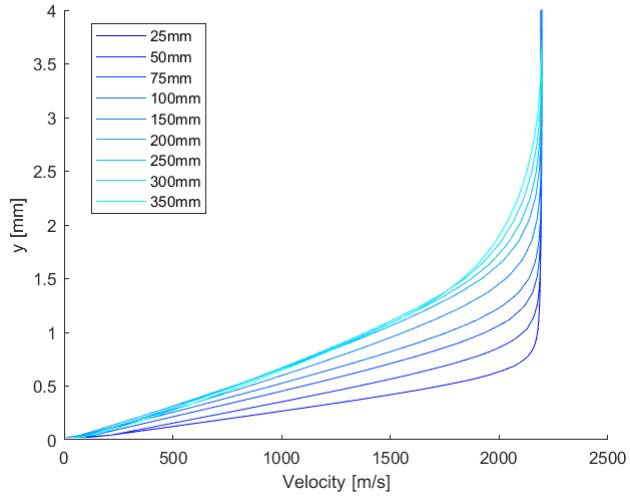

Fig. 15 Flat ramp boundary layer velocity profile, Re=E+05.

The velocity profiles of the other two isentropic ramps may be found in Appendix F. Its evident from these plots that the simulations predict on the flat ramp that the boundary layer remains entirely laminar throughout the compression ramp. Of course hypersonic flow outside the boundary layer experiences no upstream influence, however the subsonic conditions close to the wall allow for this and it is apparent that the flat ramps boundary layer develops with a very mild favourable pressure gradient - which in turn does not trigger transition for this case.

Transition is predicted for all the isentropic ramps as apparent from their velocity profiles. This is due to the mild adverse pressure gradient from the gradual turning of freestream flow across the ramps. The upstream transport of the adverse pressure gradient through the subsonic boundary layer causes an initially thick laminar formation, where it quickly transitions to a turbulent profile. The linear rate of deflection ramp appears to begin transition at approximately

150mm, where the parabolic ramp transitions at roughly 200mm and the square root rate of deflection ramp transitions between 150 and 200mm also.
A turbulent boundary layer is typically preferred in a scramjet combustion chamber as this promotes air-fuel mixing alongside the mixing caused by the shock train, therefore if the slot bleed is to be eliminated, an isentropic ramp may be preferred to initiate an adverse pressure gradient on the compression ramp, triggering boundary layer transition. Below describes the expected relative variation in boundary layer thickness given laminar to turbulent transition for a zero pressure gradient flat plate. This case is typically only seen for a subsonic flow case since a flat plate will generate pressure variations for a supersonic flow regime due to viscous displacement which generates oblique waves. Its seen that a turbulent boundary layer is typically thicker than that of the laminar case, and therefore its displacement for a zero pressure gradient. Therefore if this trend is identified upon examining the boundary layer growth across the ramps, it would be determined that its growth is highly sensitive to its profile as well as transition.

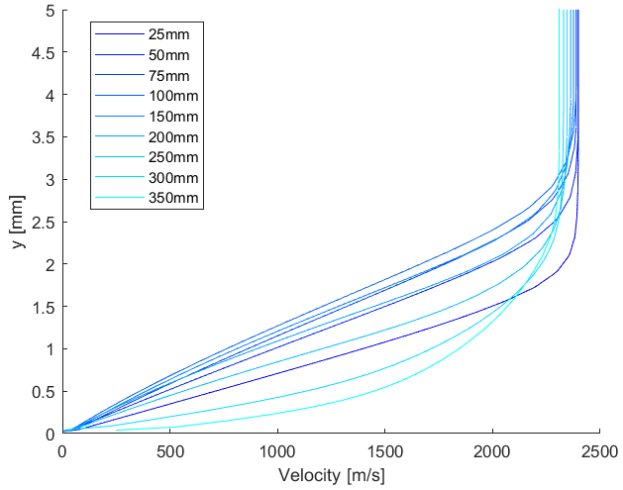

Fig. 16 Linear rate of deflection ramp boundary layer velocity profile, Re=E+05.

Boundary layer development

Below describes the development of boundary layer thickness, displacement of mass and momentum as well as the shape factor development along each ramp profile described. Its seen that the isentropic ramps do not follow the expected trend of a zero pressure gradient transitional boundary layer growth, and that in fact all aspects of the boundary layer reduce after transition. The nominal flat ramp boundary layer growth is very typical in profile and conveys what one would expect from a constant pressure field without transition.
The data suggests that all cases of isentropic turning produce smaller mass, momentum and velocity thicknesses relative to the nominal flat ramp case. In all cases, the ramp defined by the square root function aligns closest to the flat ramp case in terms of boundary layer growth, whereas the smaller initial rates of turning may be used to reduce displacement thickness of the boundary layer. The formation of the boundary layer appears to be highly dependant on the wall static pressure developed across the ramp, since the order of displacement thicknesses corresponds to the order of pressure magnitudes produced by each. Less clear relationships are found with net boundary layer thicknesses where this is found to be associated with the momentum thickness formation.
Interestingly, the parabolic rate of deflection ramp produces a parabolic boundary layer growth profile, with rapid growth and suppression of each parameter throughout the length of the ramp. The table below describes the percentage difference of each parameter at the end of the ramps relative to the values determined on the nominal flat ramp case.
From this, it is clear how each ramp profile performs in reducing each respective boundary layer profile given the same net flow deflection. The most effective ramp in reducing fluid displacement is the linear ramp where farfield displacement is reduced by 45% for this particular flow regime, with reducing the net boundary layer thickness by 23.7%. These are significant reductions in profile heights when compared to the flat ramp case, and provide evidence of effective viscous displacement reduction through manipulation of the ramps pressure distribution.
The parabolic ramp also yields significant reductions in these profiles, with being most effective at reducing the net boundary layer height by almost 40%, and displacement reduction of 35%. The boundary layer on the parabolic rate of

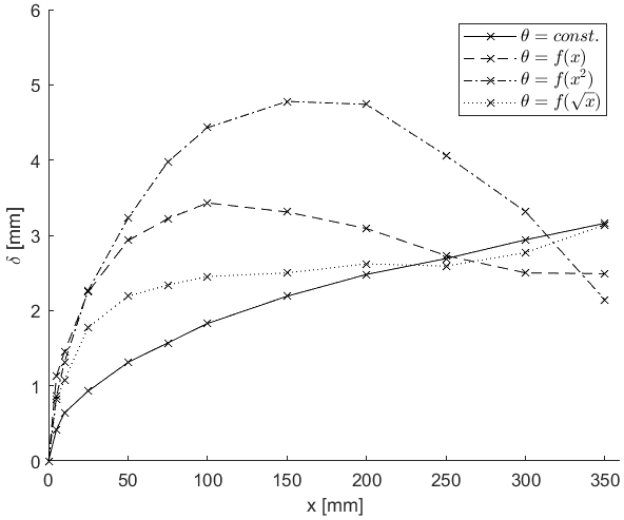

Fig. 17 Boundary layer thickness development along each investigated ramp, 2E+05.

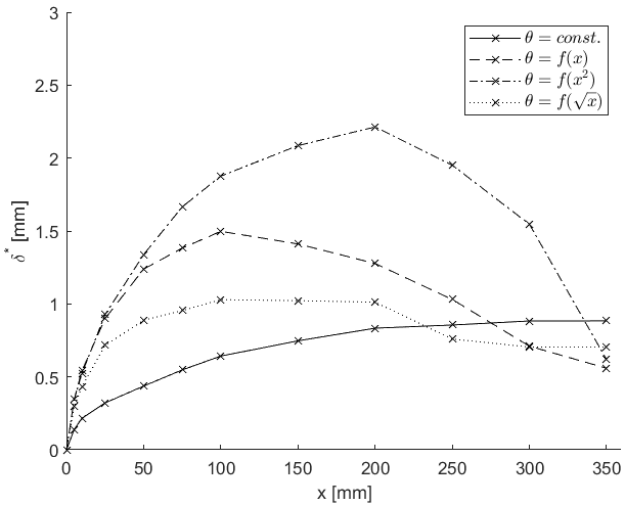

Fig. 18 Boundary layer displacement thickness development along each investigated ramp, 2E+05.

Ramp profile	δ	δ^*	θ_δ
$\theta = f(x)$	-23.717	-45.040	-22.667
$\theta = f(x^2)$	-38.491	-35.317	-30.234
$\theta = f(\sqrt{x})$	-0.635	-22.430	-1.135

Table 5 Percentage difference in boundary layer parameters relative to the nominal flat ramp case for each isentropic ramp profile.

deflection yields by far the largest magnitudes of 5mm, where its rapidly reduced as the rate of deflection increases. The shape factor plotted along the length of each ramp indicates that the flow is not at risk of separation, where momentum distribution within the boundary layer for all cases are robust and attached. This indicates that the boundary layers for all cases are suitable for expansion into the combustion chamber whilst maintaining attached flow about modest angles, reducing the risk of engine unstart.

Combustion chamber entrance flow profiles

As expected, the flat ramp generates a somewhat stable and constant pressure and temperature field to use in the

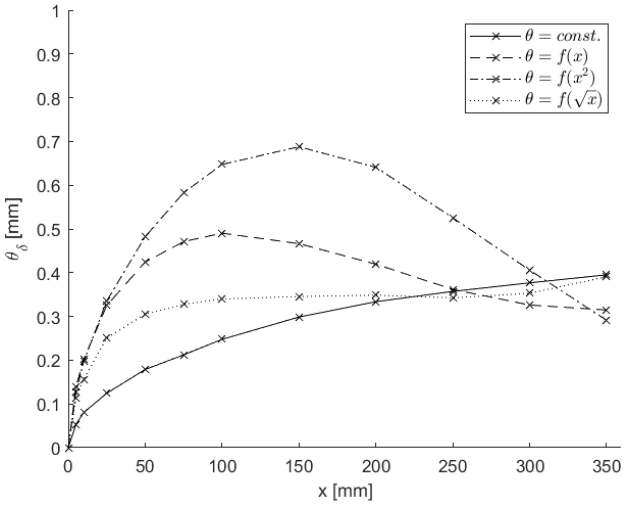

Fig. 19 Boundary layer momentum thickness development along each investigated ramp, 2E+05.

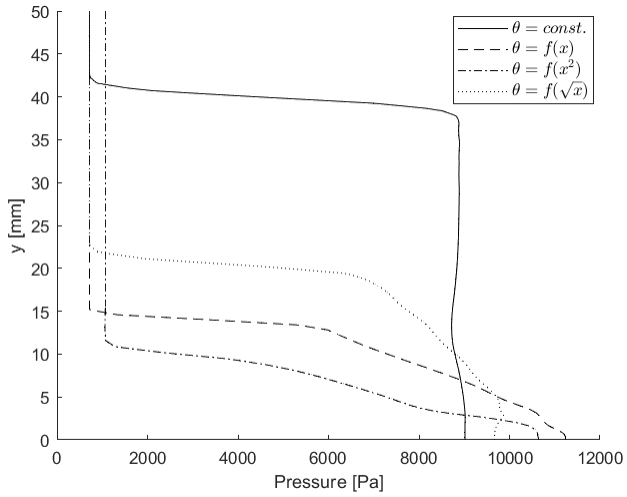

Fig. 20 Pressure profile normal to the boundary at x location 350mm for each ramp in the investigation, 2E+05.

combustion chamber. The constant angle ramp generates the largest temperatures for ensuring the autoignition of hydrogen.

Despite this, the combustion chamber is 9.8mm in height, therefore the flow conditions up to this point are only considered for suitability in use of the scramjet. Its seen that for this limit, the linear and square root rate of deflection ramps produce larger average pressures for use, increasing the potential for compression ratio in the engine, potentially increasing its thrust capacity. The optimisation of thrust in any scramjet engine is necessary to maintain constant speed in the high drag flow regime, as such a larger compression ratio is desired in such a design. The parabolic rate of deflection ramp does not appear to yield a suitable pressure profile for use in the combustion chamber since a rapid drop in pressure is experienced away from the wall, and as such is not suitable for use in such a system.

Since the square root ramp does not satisfy the desired boundary layer profiles required to satisfy mass flow requirements in the engine, the linear rate of change ramp is left as the only viable option. This ramp yields an average profile temperature between 2.5 and 9.8mm of 494K, the ideal gas approximations estimate a temperature ratio from the ramp to combustion chamber of 1.75. Given this, the linear ramp will yield a combustion chamber temperature of 864.5K, which is acceptable for the autoignition of hydrogen. Naturally a simulation of the cowl and ramp must be conducted to confirm this but it leaves the impression that the linear rate of change ramp will generate a suitable flow field for use inside of the combustion chamber.

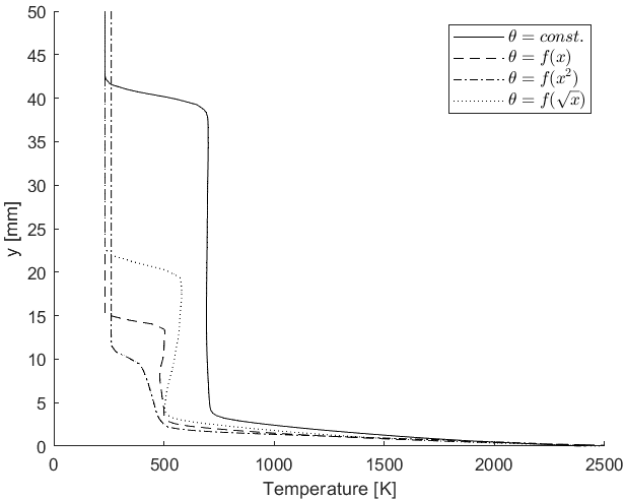

Fig. 21 Temperature profile normal to the boundary at x location 350mm for each ramp in the investigation, 2E+05.

The flowfield

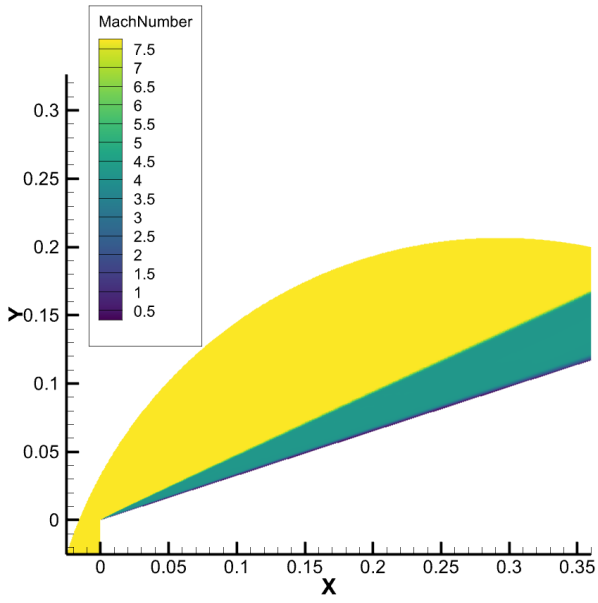

Fig. 22 Flat ramp Mach contour, Re=2E+05.

Upon visual analysis of the Mach number contours produced by the flat and isentropic ramp domains, the flat ramp generates a much larger region of influence than the gradual rate of change ramps. This may have severe consequences in terms of its application into scramjet engines since it limits the size of any combustion chamber that's used significantly. The flat ramp case generates an instant change in Mach number that remains constant throughout the field of influence. The quasi isentropic ramp however describes a gradual deceleration of the flow about it, where the final Mach number for both ramps are relatively similar. The region of influence on the gradual turning ramps was expected to be larger than what was observed, since the final turning angle was equivalent to the flat ramp. The region of influence on the ramp defined by a function of the square root shows to replicate this trend, where the field of influence is more similar to that of the flat ramp as a result of the larger initial rate of deflection.

From this data, it suggests that the largest influence on displacement thickness development on a hypersonic compression ramp for a Reynold's number of $\approx E + 05$ is the magnitude of the static pressure it produces close to the wall. It is

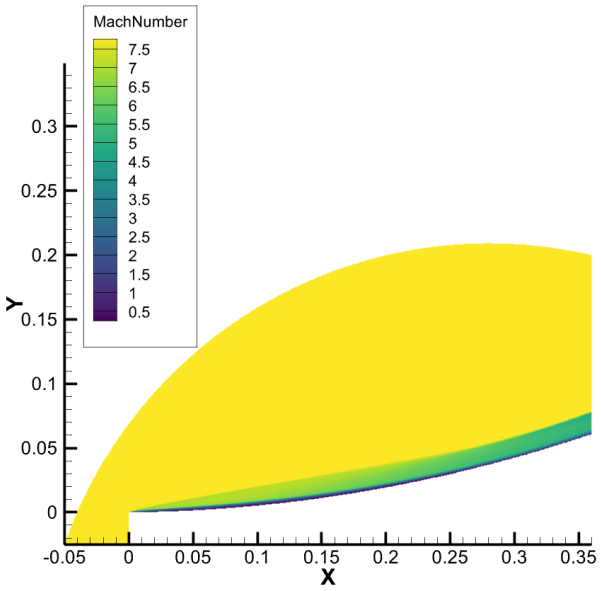

Fig. 23 Linear ramp Mach contour, Re=2E+05.

recognised that the larger static pressures produced on the isentropic ramps not only diminishes the boundary layer growth typically associated with turbulent transition, but in fact reduced net growth across the ramp when compared to the laminar boundary layer seen on the flat ramp. Considering the forces acting on a fluid element (a) close to the wall, under the influence of viscous effects; the displacement thickness describes a physical displacement of fluid away from the wall as defined by the lost mass flow rate in the boundary layer. The lost mass flow rate is a function of the fluids density and velocity tangential to the wall. The momentum integral equation as initially defined by Von Karman in 1912 describes the conservation of momentum in a compressible fluid for the direction of propagation as such [15]:

$$\int_0^{\delta} t(\rho u)\, dy + x\left(\int_0^{\delta} \rho u^2\, dy\right) - u_e x\left(\int_0^{\delta} \rho u\, dy\right) = -\tau_w - \delta p x$$

It shows that the momentum flux normal to the surface in a boundary layer is a function of the shear stress at the wall and the pressure gradient in the x direction. Its known that shear stress is a function of the fluids viscosity and therefore temperature. It would be assumed in this case that the case which generates highest wall temperatures would generated smaller shear stresses and therefore boundary layers. However that is not what appears to be the greatest influence in this flow case since the flat plate generates the highest wall temperatures and lowest pressures, it develops the largest boundary layer in all cases. Static pressure through the boundary layer is constant, and as such the fluid element (a) is in equilibrium in the y direction for a laminar boundary layer. The higher pressures generate a larger force per unit area on the wall to resist mass deficit as a result of wall shearing in the normal direction, as such develop smaller boundary layer displacements; despite adverse pressure gradients causing loss of local momentum flux close to the wall. The same could be argued for the impact on transition which would be expected.

5. Scramjet requirement qualification

The ramp defined by the square root function does not appear to generate significant reductions in boundary layer thicknesses in relation to the flat ramp, and as such will not be considered for use in further investigation.

The parabolic rate of deflection ramp, despite its extremely large initial growth of boundary layer thickness, generates good reductions in displacement and momentum thicknesses. Despite this, the pressure and temperature profiles it forms for use in the combustion chamber lack greatly in pressure and temperature characteristics, alongside a small region of disturbed flow that would barely encapsulate the cowl, its determined that this profile would not be an optimal solution for a scramjet compression ramp as seen on the Hyshot II flight experiments.

Therefore, the linear rate of deflection ramp appears to balance well the combustion chamber profiles as well as achieving the smallest displacement thickness of all test cases, and therefore will be used for further analysis. The requirements

for a scramjet intake are described in the introduction, and will be used to assess the viability of this ramp profile.

Mass flow rate requirement

Naturally, the motivation for this investigation is to ascertain whether the intrusive bleed slot seen on the Hyshot II design may be removed through means of reducing viscous displacement so that the mass flow requirement of $\dot{m}_{eff} > 0.9\dot{m}_{\infty}$. In a two dimensional flow case, this value must account for two developing boundary layers; the compression ramp and the cowl.

The need for a bleed slot is unavoidable in the flat compression ramp design when concerning the mass flow requirement. The combustion chamber is 9.8mm in height, which is limited since effective fuel mixing is required for efficient combustion. From this, the maximum displacement entering the combustion chamber must not exceed $\delta^* < 0.98$mm. The flat ramp generates a boundary layer of $\delta^*_{flat} = 0.8838$mm, which allows for a maximum of $\delta^*_{cowl} < 0.0962$mm. This is unrealistic as the length of the cowl before the combustion chamber is 4.2mm in the Hyshot II, where a value of $\frac{\delta*}{x} = 0.0229$ is unachievable in most flow regimes. Therefore the compression ramps boundary layer must have been bled as to ensure sufficient mass flow into the combustion chamber.

Now considering the linear rate of change ramp used for this investigation, the viscous displacement generated, $\delta^*_{lin} = 0.5589$mm, which would allow for $\delta^*_{cowl} < 0.0.42112$mm. Upon measurements of the cowl boundary layer that grew on the Hyshot II computational model, it generated a displacement thickness just upstream of the combustion chamber entrance of $\delta^*_{cowl} = 0.0.287$mm. Given these values, the isentropic ramp and cowl would achieve a critical condition given a 15% buffer margin.

Given these initial calculations, its concluded that the displacement reduction of the linear rate of change ramp does satisfy the mass flow requirements into the combustion chamber, allowing for critical condition to be achieved without the need for any slot bleed at all. Of course the mass flow would not be comparable to the Hyshot II design, but more importantly it does indicate that this ramp could be used in an axissymetric design as it does not require such bleed systems, which could in turn provide a larger mass flow rate per body diameter design; optimising combustion area over this initial two dimensional design.

Further study is required to justify these initial results, and to compile the ramp design into a three dimensional simulation, but the first study does suggest promise for this technique.

Compression requirement

The compression requirement outlines clearly a compression ratio of minimum 60:1 for effective combustion. The average pressures generated for the flat ramp and linear ramp up to the height of combustion chamber are given as such:

$$P_{avg,flat} = 8867.66Pa$$

$$P_{avg,lin} = 9660.12Pa$$

Its seen that the isentropic ramp, as expected, produces a larger static pressure for use in the combustion chamber, with a compression ratio of 13.5:1. Given that this ramp will be compressed further in the same manner as the flat ramp case from the cowl, it can be concluded that the linear rate of deflection ramp exceeds the compression requirements met by the flat ramp; and is therefore suitable for use in the scramjet engine.

Temperature requirement

The minimum temperature required to be achieved in the combustion chamber is 800K, this is to ensure the minimum thermal condition for autoignition of the hydrogen fuel used. The average temperatures outside of the boundary layer up to the height of the chamber are displayed below:

$$T_{avg,flat} = 696.29K$$

$$T_{avg,lin} = 493.27K$$

Its apparent that the flat ramp achieves far greater temperatures than the linear ramp for use in combustion, which leaves the concern that this ramp profile would not achieve sufficient temperatures for use in a hydrogen scramjet engine. The linear ramp would require a temperature ratio of 1.62 between the external compression ramp and the combustion chamber.

The ideal gas predictions for the flat ramp flow case predicts a cowl to combustion chamber temperature ratio of 1.75. Since this case would be similar for the linear flow case, it is apparent that the linear ramp does infact achieve the temperatures required for hydrogen combustion, and therefore is still suitable for use in the Hyshot program.

It must be stated however that despite theoretically achieving required flow conditions, the flow field generated for combustion is non constant and has small margins for thermal success. It should also be noted however that the

freestream temperature used in these simulations was 231.8K, which is perhaps some of the lowest temperatures one would expect in a typical flight regime - and as such the lower bound in freestream temperatures suggest hydrogen ignition is still viable - validating the ramp further for use in a scramjet engine.

Transition requirement

It was stated in the introduction that a turbulent boundary layer would be preferred in a combustion chamber as to promote fuel mixing by introducing turbulence intensity within it.

The potential benefit of including the linear rate of deflection into the scramjet's compression ramp is to naturally induce transition into the boundary layer without the need for trips that increase displacement thicknesses. The combination of reduced boundary layer thicknesses with a turbulent boundary layer mean that this design optimises both cases for the Hyshot II and could be a useful method for introducing boundary layer transition in a passive and non intrusive manner. Overall, the data collected in this study would suggest that the linear rate of change ramp generates a suitable flow profile for use in the combustion chamber, that would achieve effective combustion of hydrogen. The data initially suggests that this ramp may be employed without the need for any slot bleed systems for this flight regime, which in turn could translate into an axissymetric design.

6. Accounting for boundary layer compressibility

This investigation was conducted assuming that the effects of compressibility in the boundary layer are negligible, and therefore its inviscid displacement. Its seen that the density does vary within the boundary layer for the flat plate case, where the density reduces by 75% between the upper and lower regions of the boundary layer. The adjusted integral to account for compressibility is given as:

$$\rho_e u_e \delta_c^* = \int_0^{\delta} (\rho_e u_e - \rho u)\, dy$$

Below describes the difference in calculated displacement thickness for the flat plate nominal case and linear rate of deflection ramps, considering the incompressible and compressible boundary layer integral techniques.

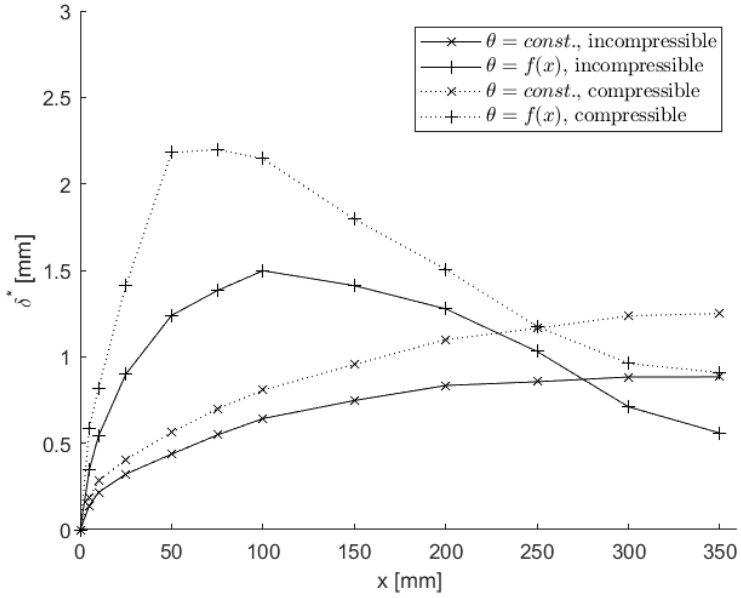

Fig. 24 Displacement thickness plotted against x [mm] for a flat plate given a compressible, and incompressible integration, Re=2E+05.

The plot shows that the incompressible assumption for this flow case predicts a lower displacement than that of the density compensated solution. This is expected since the compressible flow case experiences a lower density closer to the wall, therefore reducing mass flow in this region. The compressible calculation produces a final displacement thickness 34% larger than that for the incompressible calculation. The difference is significant and certainly could impact the application of an isentropic pressure field to operate a scramjet engine without bleed slots, however both

methods are merely indicative solutions to characterise viscous mass flow rates through a enclosed chamber - where flow choking and engine unstart are complex phenomena that are functions of more than mass flow itself. The effect of compressibility is a magnitude scalar and therefore the use of incompressible boundary layer calculations are still valid to investigate boundary layer development across different ramps.
It is clear from the plot that the difference in displacement thicknesses between the constant and linear rate of deflection ramps is consistent between the compressible and incompressible displacement thickness calculations, and as such the effect witnessed in the investigation is unaffected by compressibility in the boundary layer in terms of relative behaviour, where only the magnitudes are scaled.

7. Analytical comparisons

Its important to understand how the analytical methods for hypersonic boundary layer prediction compare in relation to the numerical solutions outlined in this investigation. Low fidelity analytical methods, if accurate enough provide a rapid form of design analysis which may be automated given a set of inputs, which cannot be said for a computational solution. The analytical solutions for this section were computed using the same methods outlined in 1.D. Below described the two methods of boundary layer prediction plotted alongside the numerical solutions of boundary layer and displacement thickness on a flat plate, Re=2E+05.

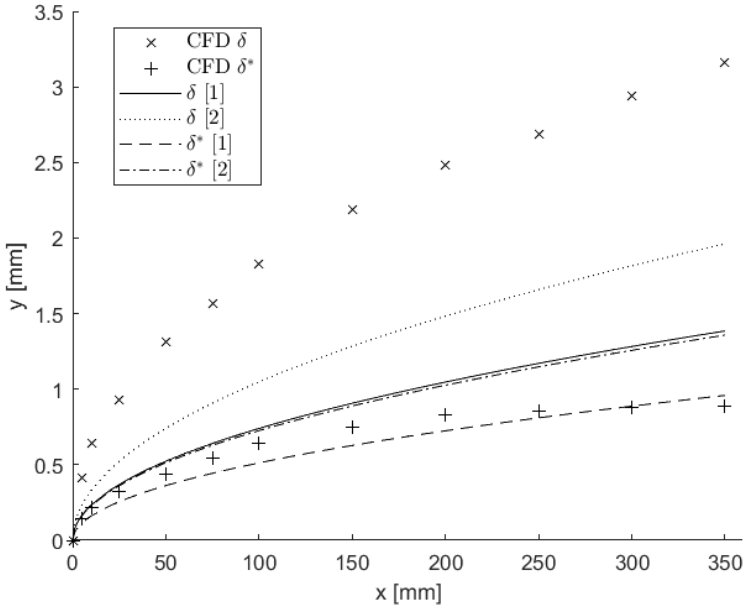

Fig. 25 Boundary layer and displacement thickness plotted against x [mm] for the flat ramp, constant pressure flow case, Re=2E+05.

Interestingly, the numerical solutions initially place midway between the two methods of calculating the displacement thickness. The initial growth is modelled well with both methods of calculation, which implies that the flow regime experiences a mostly weak viscous interaction for the sharp leading edge case. As the boundary layer develops towards the aft of the compression ramp, the analytical solution predicts a larger increase in displacement than what is found in the numerical investigation. This is thought to be a result of the difference in modelling, where the analytical model assumes a constant pressure field, and the numerical simulation generates a mildly favourable pressure gradient, resulting in lower displacement thicknesses. Its seen that the analytical assumption that the boundary layer thickness being near equivalent to that of the displacement thickness does not hold true for the numerical results. The boundary layer thickness for the flat plate appears to be greater than double that of the displacement thickness. The reasoning for the difference is unknown, but is important to acknowledge that discrepancies must be expected in this assumption when conducting analytical evaluations.
Overall, the two analytical solutions provide excellent correlation with the numerical solutions in terms of displacement thickness, and appear to outline the upper and lower bands of this growth for a flat plate for this flow case. Fig. 31

describes the pressure profiles for the linear rate of deflection isentropic ramp used in the numerical investigation, alongside that described by a theoretically isentropic pressure distribution.

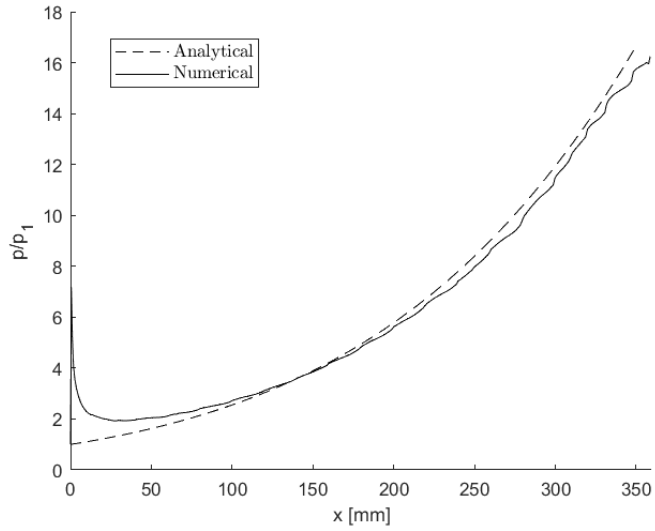

Fig. 26 Pressure ratio plotted against x for the linear rate of change ramp as well as a perfect isentropic pressure field, Re=2E+05.

The first thing to recognise is how effectively the linear rate of change compression ramp design accurately represents an isentropic pressure field. Considering that a theoretical isentropic ramp is infinite in length with the rate of deflection approaching zero, to achieve such pressure distributions in a small, finite length with finite ramp discretisation shows that this method of ramp construction is an excellent method for achieving the isentropic flow field with minimal losses on a real flow compression ramp. The losses are apparent in the small difference in pressure ratio between the two plots, even despite the shape being captured accurately. The initial divergence is the computed large pressures associated with the sharp leading edge at the wall boundary, boundary layer growth would be mostly influenced by a strong viscous interaction in this region despite this, so it would be assumed that its a simplification in mathematical modelling rather than the solver itself.

Below describes the boundary layer and displacement thickness results for the numerical simulation of the linear rate of deflection ramp and both analytical methods given a perfect isentropic pressure distribution.

More deviation is found in the isentropic investigation between the two methods than what was seen in the constant pressure results. The same trend in underestimating the net boundary layer thickness is shown, and the shape of growth is captured well, including the point at which the boundary layer growth begins to reverse. The displacement thickness between the analytical and numerical methods agree for the first half of the ramp, where the analytical methods severely under predict the extent to which the displacement thickness is reduced given an isentropic pressure field that the CFD solver predicts. Nevertheless, the trend in boundary layer growth is predicted well by this method in a more complex flowfield, where more divergence is seen in the analytical model, inferring that the analytical solutions do not predict well the extent of the effect of large pressures on displacement thickness growth.

It has been suggested from the investigations data that; for the flow regime of an experimental data point from a flight test of the Hyshot II, the viscous displacement of a fluid about the compression ramp may be effectively reduced, allowing for mass flow requirements to be met in the combustion chamber without the need for a bleed slot. It is therefore important to understand the limitations of the effect shown in this study, most notably the impact that the flight Reynold's number has on the result shown, as well as the impact on wall temperature in further reducing the boundary layer thicknesses seen.

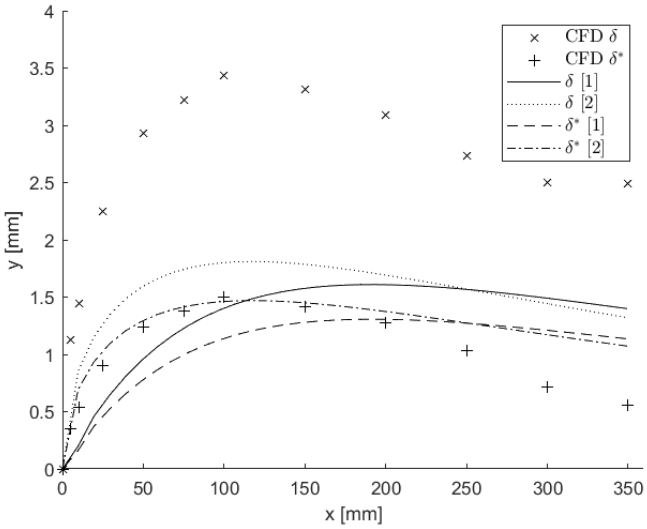

Fig. 27 Boundary layer and displacement thickness plotted against x [mm] for the analytical and numerical isentropic ramps, Re=2E+05

C. Discussion

1. Study reliability

The conclusions displayed in this investigation rely entirely on the prediction capabilities of the time averaged, steady RANS $K-\omega$ SST turbulence model in predicting the growth of a boundary layer for the given flow regime. Phenomena such as micro eddy's, localised effects of turbulence and time dependant unsteady behaviour are smoothed and not considered for the data presented. Such a turbulence model do not resolve the true nature of a real gas flow, rather they mimic the global trends experienced in the flow through use of constants in turbulent kinetic energy; which predicts the averaged energy of the turbulence of the gas, as well as constants determining the rate of turbulent dissipation; which describes the magnitude of the turbulence. Such mimicry must be approached with scepticism when considering a flow regime that is still being investigated to be modelled well with these methods.

This investigation is suited well to a RANS study, since global trends in boundary layer growth are concerned - unsteady behaviour of the hypersonic flow regime are not considered. A time averaged solution would be construed to accurately model the real gas an external compression ramp would experience - particularly in a stable flow field since oblique waves are considered stable flow systems, and the discontinuities associated with them are predictable and produce a reliable flow regime downstream of them.

The other concern them lies with whether the turbulence model used accurately predicts the growth a real gas would experience. Naturally, little is published in terms of experimental and flight test data to verify the accuracy of RANS turbulence models predicting hypersonic viscous development, so it must be validated through indirect means. The large displacement thicknesses associated with a hypersonic flow field would be assumed to have a large effect on the characteristics of the flow itself, since the magnitude of displacement on any supersonic flow directly correlates to the pressures and temperatures the flow experiences. This was the purpose of Chapter 6, where it was found that the SST turbulence model predicts the static pressure in the combustion chamber to within +6% of the flight test, and the real gas model predicts the temperature to within 2.5%. Considering that the simulation was conducted with a two dimensional domain, the solver was expected to predict a larger static pressure in the combustion chamber since the flight test would experienced an accelerated flow through it as the side walls compress the flow through it, reducing its static pressure. Even despite this, the correlation is remarkable for such a computationally inexpensive method of analysis, where the equilibrium thermal model and SST viscous predictions generate a flow regime highly correlated to that of a real gas flight test. Both the flat plate and isentropic ramps were shown to correlate well with published analytical techniques, it is from this that it may be suggested that the methods described in this project produce a reliable suggestion for boundary layer prediction for a Mach 8 flow regime on compression ramps and that the trends are suggestive for that would be seen on a real gas flow.

V. Conclusion

This research included studies into the effect of wall temperature and Reynold's number on the phenomena of passively reducing the size of a boundary layer which have not been included for the purpose of a concise article, the conclusions of this sub-investigation are nevertheless compiled below for relevance. The research performed also included a preliminary axissymetric solution which fed into a suggestion for design optimisation that is expected to be released with an extended publication.

1. A summary of the investigation's conclusions

The following conclusions have been compiled proceeding the investigation to address these objectives.

1) The viscous displacement of a hypersonic fluid can be reduced relative to a flat plate by implementing a gradual deflection about an external compression ramp.
2) The pressure distribution given a linear rate of deflection on a compression ramp may achieve a quasi isentropic pressure field effectively, for a finite and realistic ramp length.
3) Despite the introduction of an adverse pressure gradient on the compression ramp; which increases the likelihood of boundary layer transition, all facets of boundary layer growth are reduced relative to the nominal flat plate case as a result of the increased static pressure produced at the wall.
4) The investigation suggested that the effectiveness of gradual turning in reducing viscous displacement relative to the flat plate increases positively with the global Reynold's number of the flow, where for smaller Reynold's numbers the effect may be reversed.
5) Introducing a cold wall will reduce the magnitude of boundary layer growth in all cases, where the effectiveness of gradual turning is reduced for the cold wall cases. Despite the reduced effectiveness for a cold wall, a decrease in net displacement is still apparent. Therefore this technique is most effective when a wall cooling system is difficult to employ.

2. Improving the accuracy of the investigation

Whilst this investigation has highlighted key and interesting phenomena associated with boundary layer growth about a hypersonic compression ramp, the methodology has left some room for stipulation in the results which should be refined in a further investigation. The following list addresses the issues with the accuracy in this project, alongside suggestions for anyone who will attempt a follow on study.

- The same investigation should be conducted running an entirely laminar and turbulent boundary layer assumption as to eliminate the variable of boundary layer transition. Transition is famously difficult to predict, and even though its been acknowledged that the transition model used in this investigation is not a direct simulation of the transition such an intake would experience; it would be important to isolate this phenomena and determine the effect it has on the results developed in the project. This would allow the range of the effectiveness range a real gas flow would expect.
- For further study, the first order truncation error in the boundary layer integrals may be minimised by increasing the number of data points exported for the velocity profiles. This reduces Δx and therefore the error in the calculation; as the number of data points increases, this truncation error approaches zero with the same method.
- Whilst it was attempted to eliminate error by using the same mesh between investigations, the difference in boundary layer development infact induces error when the same meshes are used between these cases. A further investigation should take time to ensure the relative mesh density in the boundary layer is consistent along the ramps length, as well as scaling the node densities to be equivalent between ramp cases. This would ensure that the same resolution in the boundary layer is captured between cases and therefore the results collected would be directly comparable, where this investigation would inherit error considering this.
- Further study should also consider running an unsteady, DES or even LES simulation. The steady RANS solver does not account for the inherent unsteady and volatile nature of a hypersonic flow field, and as such important features that impact the growth of a boundary layer are averaged and dismissed in these simulations. The voritcal structures in the subsonic regions of the flow may have major implications in strong viscous regions and therefore boundary layer growth. Its known that strong shock waves, especially about a three dimensional domain induce strong vortical behaviours, and when considering a further design iteration about a cone a RANS solver is not thought to be sufficient to capture this behaviour.

Acknowledgments

We would like to acknowledge the High Performance Computing (HPC) facility at Cranfield University for the computational resources required in this project.

References

[1] UQ News, "Milestones in the history of scramjets," Office of Marketing, July 2002. URL https://www.uq.edu.au/news/article/2002/07/milestones-history-of-scramjets, [online] https://www.uq.edu.au/news/article/2002/07/milestones-history-of-scramjets.

[2] Hadjkacem, S., Jemni, M. A., Driss, Z., and Abid, M. S., "Effect of engine compression ratio on thermodynamic behavior using alternative hydrogen-LPG fuel," *DOI*, Vol. 1, 2019, p. 7.

[3] Rana, Z., Thornber, B., and Drikakis, D., "Analysis of Hydrogen Injection into the Combustor of HyShot-II Scramjet Engine Using ILES," *AIAA*, Vol. 49, 2011, pp. 4–10.

[4] UQ News, "HyShot program secures place in flight history," Office of Marketing, August 2002. URL https://www.uq.edu.au/news/article/2002/08/hyshot-program-secures-place-flight-history, [online] https://www.uq.edu.au/news/article/2002/08/hyshot-program-secures-place-flight-history.

[5] UQ News, "Early HyShot™ data encouraging that experiment proceeded," Office of Marketing, June 2007. URL https://www.uq.edu.au/news/article/2007/06/safe-launch-scramjet-experiment, [online] https://www.uq.edu.au/news/article/2007/06/safe-launch-scramjet-experiment.

[6] Hass, N. E., Smart, M. K., and Paull, A., "Flight Data Analysis of HyShot 2," *AIAA/CIRA*, Vol. 13, 2002, p. 4.

[7] Rana, Z., Thornber, B., and Drikakis, D., "Large eddy simulation of a scramjet model (Hyshot II) using high-resolution methods," *IAA/ASME/SAE/ASEE Joint Propulsion Conference Exhibit*, Vol. 45, 2009, p. 7.

[8] STOLLERY, J. L., and BATES, L., "Turbulent hypersonic viscous interaction," *Fluid Mechanics*, Vol. 63, 1974, pp. 4–25.

[9] Rana, Z., and Exposito, D., "Computational Investigations into heat transfer over a double wedge in hypersonic flows," *Aerospace Science and Technology*, Vol. 92, 2019, pp. 839–846.

[10] Cadence, "Improve CFD Accuracy with Correct Mesh Resolution," *Compute Grid Spacing for a Given Y+*, 2023. URL https://www.cadence.com/en_US/home/tools/system-analysis/computational-fluid-dynamics/y-plus.html.

[11] Siemens, "Coupled Flow Solvers Reference," *Star CCM+ guide*, Vol. 1, 2014. URL file:///C:/Program%20Files/Siemens/15.06.008-R8/STAR-CCM+15.06.008-R8/doc/en/online/index.html#page/STARCCMP%2FGUID-021347E8-7C96-4C60-A396-621DEBA08B6E.html%23.

[12] Roache, Ghia, K., and White, F., "Editorial Policy Statement on the Control of Numerical Accuracy," *ASME Journal of Fluids Engineering*, Vol. 108, 1986, pp. 1–25.

[13] Fry, R. S., *Notes on Thermodynamics, Fluid Mechanics, and Gas Dynamics*, Purdue University, West Lafayette, IN 47907-2088, U.S.A, 2023.

[14] Ye, S., *Approximate integrals using Taylor series and numerical methods*, CalTech University, 1200 E. California Blvd., Pasadena, CA 91125, 2010.

[15] Viscous flow, "The momentum integral equation," Kevin P Gary, Feb 2023. URL https://canvas.cranfield.ac.uk/courses/19361/pages/the-momentum-integral-equation?module_item_id=360727, [online] https://canvas.cranfield.ac.uk/courses/19361/pages/the-momentum-integral-equation?module_item_id=360727.

https://dspace.org/

Hypersonic boundary layer reduction with optimisation of the Hyshot II intake using numerical methods

Burrows, Sam; Rana, Zeeshan A.; Prince, Simon A.

2024-01-04
American Institute of Aeronautics and Astronautics (AIAA)
https://doi.org/10.2514/6.2024-2861
Burrows S, Rana ZA, Prince S. (2024) Hypersonic boundary layer reduction with optimisation of the Hyshot II intake using numerical methods. In: AIAA SCITECH 2024 Forum, 8-12 January 2024, Orlando, FL, USA, Paper number AIAA 2024-2861

Downloaded from a DSpace repository. https://dspace.org/